

Dipole response of ^{87}Rb and its impact on the $^{86}\text{Rb}(n, \gamma)^{87}\text{Rb}$ cross section

J. Wilhelmy^{1,*}, M. Müscher,¹ G. Rusev,² R. Schwengner,³ R. Beyer,³ M. Bhihe,^{4,5} P. Erbacher,⁶ F. Fiedler,³
 U. Friman-Gayer,^{5,7} J. Glorius,^{6,8} R. Greifehagen,³ S. Hammer,³ T. Hensel,³ J. Isaak,⁹ A. R. Junghans,³ Krishichayan,^{4,5}
 B. Löher,⁸ S. E. Müller,³ N. Pietralla,⁹ S. Reinicke,³ D. Savran,⁸ P. Scholz,^{1,†} K. Sonnabend,⁶ T. Szücs,³ M. Tamkas,^{8,10}
 W. Tornow,^{4,5} S. Turkat,¹¹ A. Wagner,³ and A. Zilges¹

¹*Institut für Kernphysik, Universität zu Köln, 50937 Köln, Germany*

²*Los Alamos National Laboratory, Los Alamos, New Mexico 87545, USA*

³*Institut für Strahlenphysik, Helmholtz-Zentrum Dresden-Rossendorf, 01328 Dresden, Germany*

⁴*Department of Physics, Duke University, Durham, North Carolina 27708, USA*

⁵*Triangle Universities Nuclear Laboratory, Durham, North Carolina 27708, USA*

⁶*Institute for Experimental Astrophysics, Goethe Universität Frankfurt, 60323 Frankfurt am Main, Germany*

⁷*Department of Physics and Astronomy, University of North Carolina at Chapel Hill, Chapel Hill, North Carolina 27599, USA*

⁸*GSI Helmholtzzentrum für Schwerionenforschung GmbH, 64291 Darmstadt, Germany*

⁹*Institut für Kernphysik, Technische Universität Darmstadt, 64289 Darmstadt, Germany*

¹⁰*Vocational School, Istanbul Kultur University, Incirli Campus, Istanbul, Turkey*

¹¹*Institut für Kern- und Teilchenphysik, Technische Universität Dresden, 01069 Dresden, Germany*



(Received 18 June 2020; revised 24 August 2020; accepted 28 September 2020; published 27 October 2020)

Background: Detailed information on the low-lying dipole response in atomic nuclei along isotonic or isotopic chains is well suited to systematically investigate the structure and evolution of the pygmy dipole resonance (PDR). Moreover, the dipole strength below and around the neutron separation energy S_n has impact on statistical model calculations for nucleosynthesis processes.

Purpose: The photon strength function (PSF) of ^{87}Rb , which is directly connected to the photoabsorption cross section, is a crucial input for statistical model calculations constraining the Maxwellian-averaged cross section (MACS) of the neutron capture of the unstable s -process branching-point nucleus ^{86}Rb . Within this work, the photoabsorption cross section is investigated.

Methods: The photoabsorption cross section of the $N = 50$ nucleus ^{87}Rb was determined from photon-scattering experiments via the nuclear resonance fluorescence (NRF) technique. Bremsstrahlung beams at the γELBE facility in conjunction with monoenergetic photon beams at the HI γ S facility were used to determine the integrated cross sections I_s of isolated states as well as the averaged cross section as function of the excitation energy. Decays to the ground state were disentangled from decays to first low-lying excited states. Statistical and experimental approaches for the γ -decay properties at various excitation energies were applied. The linearly polarized photon beams at HI γ S provide information on the ratio of electric and magnetic type of radiation.

Results: Within this work, more than 200 ground-state decays and associated levels in ^{87}Rb were identified. Moreover, transitions below the sensitivity limit of the state-by-state analysis were taken into account via a statistical approach from the bremsstrahlung data as well as model-independently from the HI γ S data. The photoabsorption cross sections at various excitation energies were determined. The dipole response between 6 and 10 MeV of ^{87}Rb is in agreement with assuming contributions of electric multipolarity, only.

Conclusions: The photoabsorption cross section of ^{87}Rb does not contradict with the trend of decreasing $E1$ strength with increasing proton number along the $N = 50$ isotonic chain but might also be associated with a constant trend. The experimental γ decay at various excitation energies of the HI γ S data supports the statistical approach but does not provide a stringent proof due to the limited sensitivity in the decay channels. The additional $E1$ strength observed in the present experiments significantly enhances the MACSs compared only to recent microscopic HFB+QRPA (Hartree-Fock-Bogoliubov plus quasiparticle random-phase approximation) calculations using the D1M interaction. Moreover, theoretical estimations provided by the KADoNiS project could be significantly improved.

DOI: [10.1103/PhysRevC.102.044327](https://doi.org/10.1103/PhysRevC.102.044327)

*wilhelmy@ikp.uni-koeln.de

†Present address: Department of Physics, University of Notre Dame, Indiana 46556-5670, USA.

I. INTRODUCTION

Electric dipole ($E1$) and magnetic dipole ($M1$) excitations are fundamental modes observed in atomic nuclei [1,2]. The electric dipole response is dominated by the giant dipole resonance (GDR) [3] that contributes almost 100% to the Thomas-Reiche-Kuhn (TRK) sum rule [4,5]. To shed light on the evolution of the GDR with, e.g., increasing neutron-proton asymmetry and emerging deformation, a variety of systematic studies along the nuclear chart was performed during the last decades; see, e.g., Refs. [6–10]. Its Lorentzian resonance centroid-energy lies well above the neutron separation energy. Studies for many nuclei proved that a simple extrapolation of the GDR to lower energies does not fully describe the low-lying $E1$ strength [1]. Enhanced $E1$ strength around and below the neutron separation energy is commonly denoted as pygmy dipole resonance (PDR) and is sometimes described as a neutron-skin oscillation against an isospin-saturated core [1]. In this simple approach, the pygmy strength is expected to correlate with the neutron-skin thickness of atomic nuclei. Therefore, studies along isotopic and isotonic chains yield information on the evolution with changing proton-to-neutron asymmetry. Such investigations were performed, e.g., for the Sn isotopes [11–17], the Xe isotopes [18], the $A = 50$ mass region [19–28], the $N = 82$ isotones [29–34] and the $N = 50$ isotones [35–39]. In the $N = 50$ chain the photoabsorption cross sections above 6 MeV for all stable nuclei besides ^{87}Rb were measured [35–39].

In most spherical even-even nuclei, the energetically lowest (usually below $E_x = 5$ MeV) $E1$ contribution is generated by the two-phonon $(2_1^+ \otimes 3_1^-)_1$ -dipole excitation [40]. In odd-even nuclei the respective excitation is fragmented by the coupling to the unpaired valence particle $(2_1^+ \otimes 3_1^- \otimes \text{particle})$.

Within the last years enormous effort was made to disentangle the underlying structures that contribute to the low-lying $E1$ strength. For the pygmy region above about 5 MeV it turned out that complementary probes may provide detailed information on the properties of excitation modes. Two parts of low-lying $E1$ strength have been disclosed by a multimessenger approach for some nuclei (^{124}Sn [14], ^{138}Ba [41], ^{140}Ce [41,42]) which is referred to as isospin splitting [43,44].

Moreover, information on the excitation energy of excited states as well as their γ -decay behavior yield information on their underlying structure. For example, for the above-mentioned two-phonon excitation the $B(E2)$ strength for the $1_1^- \rightarrow 3_1^-$ transition should equal that of the $2_1^+ \rightarrow 0_1^+$ transition. A direct observation of this transition is experimentally challenging for most cases because of its weak branching. However, for some cases a direct identification was possible, e.g., for ^{40}Ca [45] or nuclei in the $N = 82$ chain [46,47]. An additional signature of this two-phonon state is its excitation energy which is slightly below ($\approx 90\%$) the sum of the 2_1^+ and 3_1^- states. Several candidates for two-phonon excitations $(2_1^+ \otimes 3_1^- \otimes \text{particle})$ were identified within the last years [48].

As the PDR is located in the vicinity of the neutron separation threshold, it has an impact on statistical model calculations of neutron-capture cross sections and nucleosyn-

thesis processes [49]. The photon strength function (PSF), which is directly connected to the photoabsorption cross section, is a crucial input for predictions of neutron-capture reaction rates [50]. Their correlation has been demonstrated in several publications; see, e.g., Refs. [51–57].

The relative abundance of Rb to Sr, Y, or Zr yields information on the neutron density in the s process [58,59] and the $^{86}\text{Rb}(n, \gamma)^{87}\text{Rb}$ cross section is a minor branching point. However, only 22% of the solar abundance of Rb can be assigned to the s process [60]. The isotope ^{85}Rb is stable and has a large neutron capture cross section of 234(7) mb [61]. Therefore, especially ^{85}Rb can be ascribed to the r process (92% of solar ^{85}Rb). Because of the $N = 50$ shell closure the neutron-capture cross section of ^{87}Rb is relatively small (15.7(8) mb) [61]. Hence, if the branching points at ^{85}Kr and ^{86}Rb are activated the very long-lived isotope ^{87}Rb ($T_{1/2} = 4.97(3) \times 10^{10}$ yr [62]) can be significantly produced. The ^{22}Ne source is activated in the massive asymptotic giant branch (AGB) model and branching points are open due to the high neutron density. In contrast, in the low-mass AGB model, where the ^{13}C neutron source is activated, branching points are closed because of the lower neutron densities. Therefore, the abundance of ^{87}Rb enables the test of theoretical s -process abundances in s -process enhanced stars. This is especially true for Rb because it can be spectroscopically identified.

The s -process waiting-point nucleus ^{86}Rb is unstable, and a direct measurement of the (n, γ) cross section is not feasible [58]. Therefore, a precise knowledge of the PSF of ^{87}Rb is important to improve statistical model calculations and constrain predictions of the nucleosynthesis in the s process in the $A = 90$ mass region. A more detailed description can be found in Refs. [58,59,63].

In this work we will present experimental results on the dipole response of ^{87}Rb analyzed from complementary nuclear resonance fluorescence (NRF) measurements using continuous-energy bremsstrahlung with maximum energies of 8.2 and 13.2 MeV as well as linearly polarized monoenergetic photon beams at 18 beam-energy settings covering the energy region of 5.1 to 9.6 MeV.

II. EXPERIMENTAL METHOD AND SETUPS

Photons dominantly induce $E1$ and $M1$ excitations and, therefore, nuclear resonance fluorescence (NRF) measurements are well suited for the investigation of the dipole response of atomic nuclei with high sensitivity. Excitation energies E_x , integrated cross sections I_s , and partial decay widths Γ_i of isolated nuclear states can be extracted in a model-independent way [40]:

$$I_s = \int \sigma_{\gamma\gamma} dE = \pi^2 \left(\frac{\hbar c}{E_x} \right)^2 g \frac{\Gamma_0 \Gamma_f}{\Gamma}. \quad (1)$$

Here, g is the spin factor and is defined by $g = (2J_i + 1)/(2J_0 + 1)$ where J_i and J_0 denote the spins of the excited state and the ground state, respectively. Excited states can either decay back directly to the ground state (*elastic* transitions), i.e., $J_0^\pi \xrightarrow{\gamma_0} J_i^\pi \xrightarrow{\gamma_1} J_0^\pi$ or via intermediate states (*inelastic* transitions), i.e., $J_0^\pi \xrightarrow{\gamma_0} J_i^\pi \xrightarrow{\gamma_1} J_f^\pi \xrightarrow{\gamma_2} \dots \xrightarrow{\gamma_n} J_0^\pi$. In

the following γ_1 will be denominated as *primary* decay, whereas $\gamma_2, \dots, \gamma_n$ are called *secondary* transitions.

Angular distributions $W(\theta, \phi)$ of emitted γ rays depend on the ground-state spin quantum number J_0^π and the spin quantum numbers of the excited state (J_i^π) and the final state (J_f^π). For unpolarized bremsstrahlung beams angular distributions are independent of the azimuthal angle ϕ . For ground-state transitions in even-even nuclei the intensity ratios of $W(\theta = 90^\circ)$ and $W(\theta = 127^\circ)$ are 0.71 and 2.26 for $J = 1$ states and $J = 2$ states, respectively, which enables a clear identification of spin quantum numbers. However, for $J \neq 0$ ground-state spins, angular distributions become less distinct. In the odd-even nucleus ^{87}Rb with ground-state spin and parity quantum number $J^\pi = 3/2^-$, states with $J^\pi = 1/2^\pi, 3/2^\pi, 5/2^\pi$ are excited via dipole transitions. For ground-state transitions, i.e., the cascade $3/2^- \rightarrow J_i^\pi \rightarrow 3/2^-$, an isotropic distribution is observed for $J_i^\pi = 1/2^\pi$, whereas $W(\theta = 90^\circ)/W(\theta = 127^\circ) \approx 0.92$ is expected for $J_i^\pi = 3/2^\pi$ and $J_i^\pi = 5/2^\pi$. Here, excited states with positive (negative) parity quantum number are populated via $E1$ ($M1$) transitions.

For linearly polarized photon beams, angular distributions $W(\theta, \phi)$ are sensitive to the parity quantum number, and ϕ denotes the azimuthal angle with respect to the polarization plane. Consequently, the analyzing power Σ is defined by [31]

$$\Sigma = \frac{W(90^\circ, 0^\circ) - W(90^\circ, 90^\circ)}{W(90^\circ, 0^\circ) + W(90^\circ, 90^\circ)} \quad (2)$$

For the cascade $0^+ \rightarrow 1^{-(+)} \rightarrow 0^+$ the analyzing power Σ is -1 ($+1$), which allows a clear identification of the excited states' parity quantum numbers in all even-even nuclei. For the transition cascade $3/2^- \rightarrow J_i^\pi \rightarrow 3/2^-$ analyzing powers of $\Sigma = 0$ ($J_i^\pi = 1/2$), $\Sigma = \pm 0.26$ ($J_i^\pi = 3/2^\mp$), and $\Sigma = \pm 0.23$ ($J_i^\pi = 5/2^\mp$) are observed.

The sensitivity of the detection setup is given by q , which takes, e.g., the detectors' solid angle and the degree of polarization into account. The experimental azimuthal asymmetry A of emitted photons is defined by [31,40]

$$A = \frac{I_{\parallel} - I_{\perp}}{I_{\parallel} + I_{\perp}} = q\Sigma. \quad (3)$$

I_{\parallel} and I_{\perp} denote the γ -ray intensities in the detectors parallel and perpendicular to the plane of polarization.

Two NRF bremsstrahlung measurements at electron energies of 13.2 and 8.2 MeV were performed at the photon-scattering facility at the superconducting electron accelerator ELBE (γ ELBE) [64] in Dresden, Germany. For the 13.2 (8.2) MeV measurement 2478.8 (1302.2) mg Rb_2CO_3 was used and 335.9 (400) mg of the calibration standard ^{11}B was added in front of the target. The rubidium carbonate was highly enriched in ^{87}Rb ($>99\%$). Four high-purity Germanium (HPGe) semiconductor detectors with 100% efficiency relative to a $7.62 \text{ cm} \times 7.62 \text{ cm}$ NaI detector were mounted around the target. For the 13.2 MeV measurement two detectors were placed at $\theta = 90^\circ$ and $\theta = 127^\circ$ each. For the 8.2 MeV measurement all detectors were mounted at backward angles where $W(127^\circ) = 1.00$ is expected for all dipole excitations ($J_i^\pi = 1/2^\pm, 3/2^\pm, 5/2^\pm$).

The bremsstrahlung spectra at γ ELBE were produced by electron beams at kinetic energies of 13.2 and 8.2 MeV

impinging on a radiator foil consisting of $7 \mu\text{m}$ niobium for both measurements. The average electron currents were 0.5 and 0.75 mA, respectively. The time of irradiation was ≈ 260 (≈ 140) h for the measurement at $E_e^- = 13.2$ MeV ($E_e^- = 8.2$ MeV). For the higher electron energy a 10 cm thick aluminum absorber was placed behind the radiator to reduce the photon flux at lower energies. At the High Intensity Gamma-ray Source (HI γ S) facility at the Triangle Universities Nuclear Laboratory (TUNL), Durham, NC, USA [65] dipole excitations of ^{87}Rb were investigated by means of linearly polarized and quasimonoenergetic photon beams generated by the laser Compton backscattering technique. The γ -ray beam was collimated by a lead cylinder with a length of 30.5 cm and a radius of 9.525 mm.

The dipole response was measured below the neutron separation energy of ^{87}Rb at $S_n = 9.92$ MeV for 18 photon-beam energies at 5.10, 5.30, 5.50, 5.75, 6.00, 6.25, 6.50, 6.75, 7.00, 7.25, 7.50, 7.80, 8.10, 8.40, 8.70, 9.00, 9.30, and 9.60 MeV for about four hours each.

Deexciting γ rays were detected with the high-efficiency setup γ^3 [66]. Four $\text{LaBr}_3:\text{Ce}$ (LaBr) scintillator detectors and four HPGe detectors were mounted around the target, which consists of 2478.8 mg Rb_2CO_3 highly enriched in ^{87}Rb ($>99\%$) (the same target as for the 13.2 MeV measurement at γ ELBE). Two detectors of each type were placed at $\theta = 90^\circ$, one of each type in the polarization plane and one of each type out of the polarization plane, which enables the measurement of the experimental azimuthal asymmetry A . The other four detectors were mounted at $\theta = 135^\circ$ (LaBr and HPGe at $\phi = \pm 45^\circ$ and $\phi = \pm 135^\circ$, respectively).

III. DATA ANALYSIS AND RESULTS

A. State-by-state analysis of γ ELBE and HI γ S data

Measured HPGe spectra at γ ELBE are shown in Fig. 1. For excitation energies above the neutron separation threshold γ decays become weaker, because neutron emission dominates the decay. Thus, above $E_x = 10$ MeV HPGe spectra of both angles were added up to increase the sensitivity. For the measurement at $E_e^- = 8.2$ MeV all detectors were mounted at $\theta = 127^\circ$.

The full-energy detection-efficiency of the HPGe detectors was measured with a standard calibration source ^{226}Ra up to ≈ 2 MeV. At higher energies the detection-efficiency was simulated with the GEANT4 framework [67–69]. The reliability of the simulation was tested in former experiments with the same setup using high-energetic transitions in ^{11}B and ^{16}O ; for details see Ref. [36].

The electron energies were measured by the irradiation of a deuterated polyethylene film with bremsstrahlung. The protons emitted after deuteron breakup were measured with four silicon detectors of $30 \mu\text{m}$ thickness where the endpoint energy of the continuous proton spectrum provides information on the highest photon energy of the bremsstrahlung spectra [64]. The photon-flux distributions for the resulting electron energies of $E_e^- = 13.2$ MeV and $E_e^- = 8.2$ MeV were determined using the Roche function and so-called Schiff formula, respectively [64,70,71]. For the determination

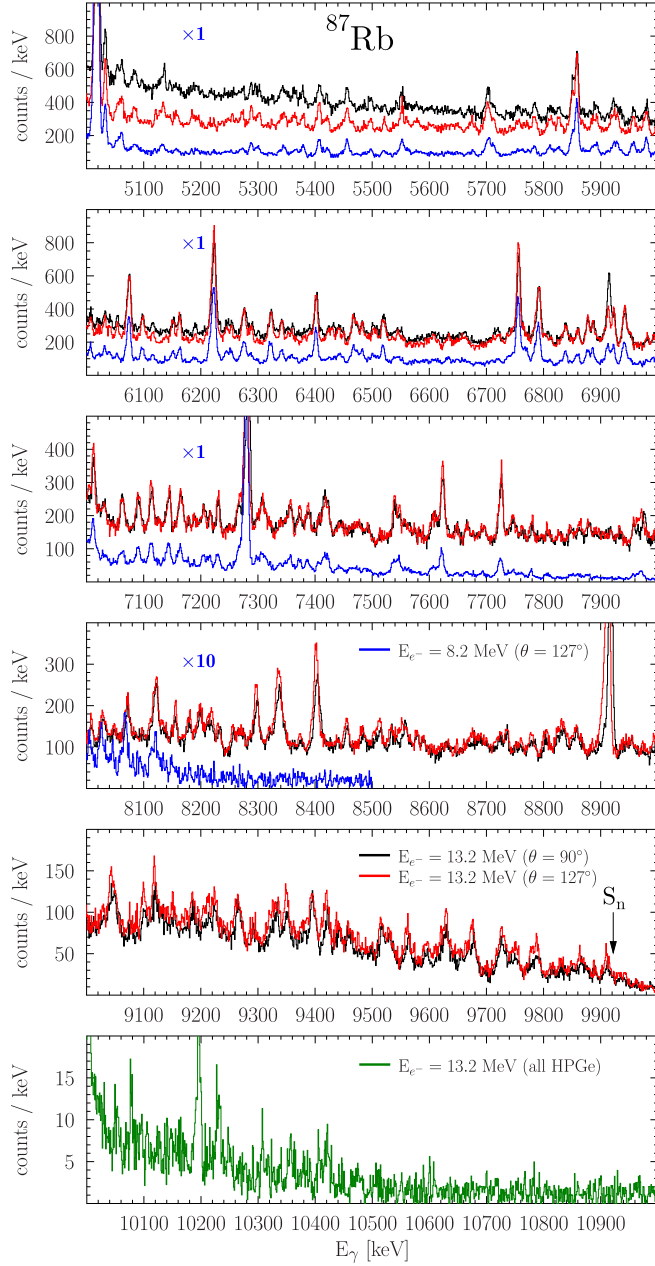


FIG. 1. HPGe spectra for the bremsstrahlung measurement at $E_{e^-} = 13.2$ MeV are illustrated in black ($\theta = 90^\circ$) and red ($\theta = 127^\circ$). Above the neutron separation threshold $S_n = 9.92$ MeV spectra of detectors at both angles are added to increase the sensitivity (shown in green). The sum of all HPGe spectra ($\theta = 127^\circ$) at $E_{e^-} = 8.2$ MeV is shown in blue.

of absolute photon fluxes at target position, photon-flux distributions were scaled to well-known transitions of the ^{11}B standard and a systematic uncertainty of $\approx 5\%$ was observed from the scaling. Angular distributions for the observed transitions in ^{11}B were determined under consideration of their multipole-mixing ratio δ [72]. The absolute photon fluxes are depicted in Fig. 2.

Integrated cross sections I_s of ^{87}Rb for isolated states were determined from both bremsstrahlung measurements to

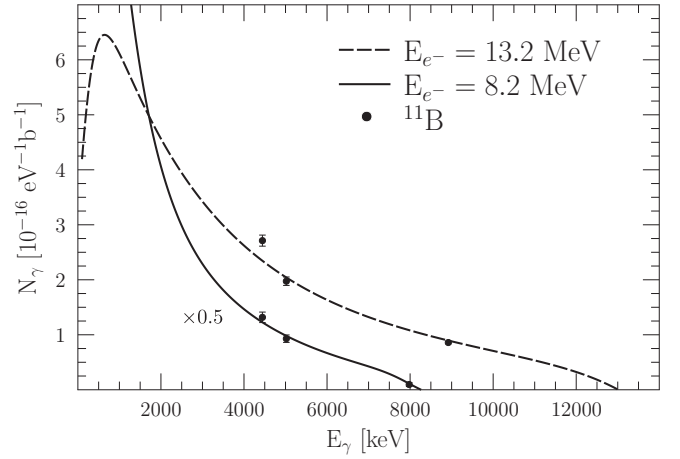


FIG. 2. The absolute photon fluxes are illustrated for the measurements at $E_{e^-} = 13.2$ MeV and $E_{e^-} = 8.2$ MeV with dashed and solid lines, respectively. The calibration points of ^{11}B are illustrated with dots.

account for feeding contributions of higher-lying excitations. The integrated cross sections I_s are associated with the excitation from the ground state via the ground-state width Γ_0 . If higher-lying excited states populate lower-lying excited states via *inelastic* transitions these lower-lying states are not purely excited from the ground state anymore. Therefore, associated intensities of the lower-lying excited states become larger and contaminate observed values for I_s . The ratio of integrated cross sections I_s at different electron energies is illustrated in Fig. 3. The ratio between the measurements at $E_{e^-} = 13.2$ MeV and $E_{e^-} = 8.2$ MeV indicates no feeding contribution of excited states above ≈ 5 MeV for the high-energy measurement. Below ≈ 5 MeV excited states seem to be significantly fed by higher-lying states. Similar observations were made by Schwengner *et al.* for other $N = 50$ nuclei [36–38]. Additionally, integrated cross-sections of the measurement at

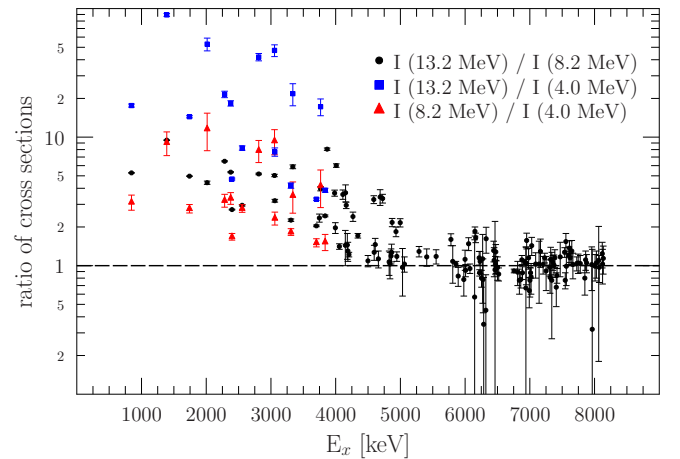


FIG. 3. The ratio of energy-integrated cross sections I_s is illustrated for bremsstrahlung measurements at different endpoint energies. Data from the $E_{e^-} = 4$ MeV measurement are taken from Ref. [73]. For details see text.

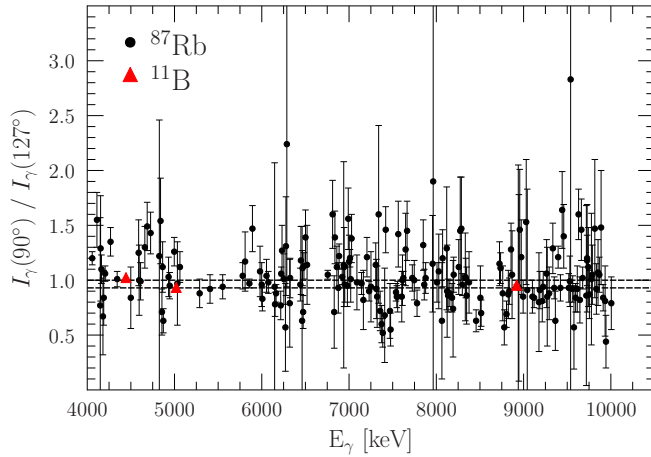


FIG. 4. Ratios of intensities $I_\gamma(90^\circ)/I_\gamma(127^\circ)$ for the $E_{e^-} = 13.2$ MeV bremsstrahlung measurement. The intensity ratios of transitions in ^{87}Rb and the calibration standard ^{11}B are illustrated with black dots and red triangles, respectively. Both nuclei have the same ground-state spin and parity quantum number ($J^\pi = 3/2^-$). For details see text.

$E_{e^-} = 8.2$ MeV are compared to a former low-energy measurement ($E_{e^-} = 4.0$ MeV) performed by Käubler *et al.* [73]. Only small feeding contributions are observed for excited states around 4 MeV, whereas the feeding contribution increases towards lower excitation energies. Following these observations integrated cross sections I_s of ^{87}Rb above 8.0 MeV, and between 4.0 and 8.0 MeV are calculated from the high-energy measurement at $E_{e^-} = 13.2$ MeV and the measurement at $E_{e^-} = 8.2$ MeV, respectively. The integrated cross sections I_s of the high-energy measurement were determined with the detectors positioned at $\theta = 127^\circ$, because the angular distribution is 1 for all intermediate spins of the observed cascades. In this way, systematic errors of different angular distributions for different spin cascades at $\theta = 90^\circ$ are avoided. The results are listed in the Supplemental Material [74].

Intensity ratios $I_\gamma(\theta = 90^\circ)/I_\gamma(\theta = 127^\circ)$ were analyzed by the measurement at $E_{e^-} = 13.2$ MeV only. The results are illustrated in Fig. 4. For dipole transitions in ^{87}Rb , isotropy (for $J_i^\pi = 1/2^\pi$) or $I_\gamma(\theta = 90^\circ)/I_\gamma(\theta = 127^\circ) = 0.92$ (for $J_i^\pi = 3/2^\pi$ and $J_i^\pi = 5/2^\pi$) is expected, as introduced in Sec. II. Because the intensity ratios for all of those three spin cascades are close to or equal to 1, a clear assignment of the spin quantum numbers is not possible. The intensity ratio for the calibration standard ^{11}B (which has the same ground-state spin of $J_i^\pi = 3/2^-$) is also depicted in Fig. 4. The complementary measurement at HI γ S using almost monoenergetic photon beams enables a clear distinction between transitions to the ground state (*elastic* transitions) and to excited states (*inelastic* transitions). The full-energy detection efficiency of the detectors of the γ^3 setup was measured with standard calibration sources ^{56}Co , ^{60}Co , and ^{137}Cs up to ≈ 3.4 MeV. At higher energies the detection efficiency was simulated with the GEANT4 framework [67–69]. As the width of the γ -ray beam profile is compar-

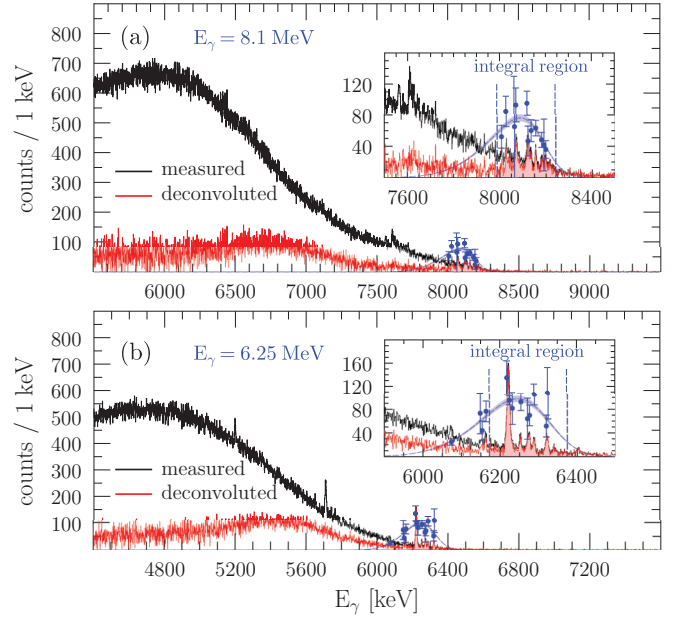


FIG. 5. HPGc sum spectra are shown for beam-energy settings at $E_\gamma = 8.1$ MeV (a) and $E_\gamma = 6.25$ MeV (b) in black. The spectra corrected for detector response are shown in red. The dashed blue lines illustrate the beam profiles that are scaled to excited states of the target nucleus ^{87}Rb (blue dots). The elastic part of the photoabsorption cross section is determined by the integrated intensity of the deconvoluted spectra shown in shaded red. For details see text.

ble to the excitation energy of the first excited state in ^{87}Rb ($E_x = 403$ keV)—at least for beam-energy settings below 8.1 MeV—all transitions observed within the beam-energy profile, which serves as an energy-selective excitation window, can be unambiguously identified as *elastic* transitions and, consequently, can be distinguished from *inelastic* transitions. Thus, a clear assignment is possible for all transitions that were observed both at γELBE and HI γ S. Associated levels are listed in the Supplemental Material [74].

Moreover, experimental azimuthal asymmetries A [see Eq. (3)] for the most dominant transitions allow the assignment of possible spin and parity quantum numbers of excited states. The value for A was only determined if the relative statistical uncertainty of the analyzed transitions was below 30% in both spectra, i.e., in and out of the plane of polarization.

The γ -ray beam profile at HI γ S is measured with a 123% HPGc detector (beam detector) that can be moved into the beam line. The absolute photon flux can be determined by the integrated cross sections I_s of isolated states of the target nucleus that were previously determined in bremsstrahlung; see Fig. 5. A detailed description of this method can be found in, e.g., Ref. [34]. The photon-flux calibration is illustrated for two beam-energy settings at 8.1 and 6.25 MeV in Figs. 5(a) and 5(b), respectively. The excited states for the photon-flux calibration at HI γ S, however, have to be selected very carefully as deexciting γ rays might overlay with single-escape events or inelastic transitions in the bremsstrahlung spectra or leaking from contaminations, e.g., of the calibration standard ^{11}B . This becomes obvious from Fig. 5(b), where, e.g., the

transition at 6402 keV was not used for the calibration due to its overlap with the single-escape line of the 6915 keV transition (^{16}O) in bremsstrahlung with $E_\gamma = 6404$ keV. The elastic cross sections for these transitions are analyzed from the HI γ S data and are marked accordingly in the Supplemental Material [74].

The uncertainties for the photon-flux calibrations are between 3% and 20% for all beam-energy settings between 5.1 and 9.3 MeV. For the highest beam energy at 9.6 MeV, the strength is highly fragmented and, thus, the uncertainty for the photon flux increases to 43% using isolated states for the calibration. The highest-lying inelastic transition is expected to be around 9.6 MeV ($S_n - 403$ keV). The energy range up to S_n covered by the HI γ S measurement is not complete. Therefore, all transitions in this energy region that were observed only at γ ELBE are also listed in the Supplemental Material [74] and are marked accordingly. Moreover, no measurements for beam-energy settings below 5.1 MeV were performed at HI γ S. Therefore also all transitions between 4 and 5 MeV that were observed at γ ELBE only are listed in the Supplemental Material [74]. In contrast to the highest energies it should be clearly stated that these transitions were not unambiguously identified as *elastic* transitions.

At lower excitation energies (≤ 4 MeV) the level density decreases and γ rays can be clearly associated with excited levels also from bremsstrahlung data only. Thus, γ -decay branching ratios are determined for the first excited states from the $E_{e^-} = 8.2$ MeV measurement. The results are listed in the Supplemental Material [74]. As first excited states are significantly fed by higher-lying states, angular distributions become isotropic. The uncertainties include statistical uncertainties only.

B. Analysis of photoabsorption cross sections

The state-by-state analysis is limited by the sensitivity limit of the HPGe detectors. In previous publications, different approaches were applied for both bremsstrahlung beams and monoenergetic beams to account for the transitions that are not accessible by a state-by-state analysis; see, e.g., Refs. [34,75,76]. For the other $N = 50$ isotones a large contribution of weak excitations below the sensitivity limit was extracted [35–38]. To integrate ^{87}Rb in the systematics of the $N = 50$ chain, it is of utmost importance to take unresolved strength into account. In the present approach we will unify two complementary methods. First, the photoabsorption cross section will be determined from the HI γ S data in a model-independent way. Second, the photoabsorption cross section will be extracted directly from the bremsstrahlung data using a statistical approach.

As all transitions within the beam-energy window at HI γ S are ground-state transitions, the total intensity in this excitation region yields the elastic cross section (besides the low-energy part of the beam profile for higher photon-beam energies). For this purpose, the detector responses of the HPGe detectors of the γ^3 setup were simulated with GEANT4 Monte Carlo simulations [66–69]. The geometry of this setup is well known and detector properties have been intensively studied in previous experiments; see, e.g., Refs. [34,66,77].

However, this approach is limited in the present work as the vacuum in the beam pipe was insufficient. Hence, beam-induced background is observed at high energies resulting from small-angle scattering off the rest gas. The effect of insufficiently evacuated beam pipe is illustrated in Ref. [66]. The contribution of this background becomes obvious by a direct comparison of the spectra from this work, see Fig. 5, to the spectra of the measurements on, e.g., ^{52}Cr [27], ^{86}Kr [38], or ^{140}Ce [34] with a similar setup. Due to the energy loss during the scattering process the high-energy part of the beam profile is less affected. Thus, only the integrated intensity from the lower integral limit $l = E_{\text{beam}} - \text{FW3/4M}$ to the upper integral limit $r = E_{\text{beam}} + \text{FW1/4M}$ in the deconvoluted HPGe spectra was used; see Fig. 5. FW3/4M (FW1/4M) denotes the value for the γ -ray energy where the intensity of the beam profile is decreased to 3/4 (1/4) of the maximum value. A similar approach was done for ^{130}Te where the measured spectrum (i.e., not the deconvoluted spectrum) was integrated only above $E_{\text{beam}} - 1\sigma_{\text{beam}}$ to take unresolved transitions into account [76]. For the present work, it should be clearly emphasized that the intensity that is associated with the elastic cross section might be contaminated by this background. As illustrated in Fig. 5, the intensity of the deconvoluted spectrum does not approach zero at the low-energy part of the profile. It should be pointed out that this intensity can also be associated with the decay to the first excited state at 403 keV and is overlaying with the beam-induced background. Thus, no empirical function can be assigned to the background. To exclude an assignment of decays to $E_x = 403$ keV as ground-state transitions and to reduce the influence of the beam-induced background, the restriction of the integral region is mandatory.

The LaBr detectors were placed closer to the target compared to the HPGe detectors. Therefore, beam-induced background might result from smaller scattering angles in the rest gas and might affect higher parts of the beam profile. As the statistical uncertainties of the integrated volume in the HPGe detectors are well below 3% for all beam-energy settings above 6 MeV the better detection efficiency of the LaBr detectors will not improve statistical uncertainties (that is dominated by the photon-flux calibration) and, thus, the LaBr detectors were not used.

The total cross section σ_γ is the sum of the. The average branching ratio to the ground state $\langle b_0 \rangle$ is defined via the *elastic*, *inelastic*, and total cross sections $\sigma_{\gamma\gamma}$, $\sigma_{\gamma\gamma'}$, and σ_γ :

$$\langle b_0 \rangle = \frac{\sigma_{\gamma\gamma}}{\sigma_{\gamma\gamma} + \sigma_{\gamma\gamma'}} \cong \frac{\sigma_{\gamma\gamma}}{\sigma_\gamma}. \quad (4)$$

As *inelastic* transitions populate lower-lying excited states the *inelastic* cross section $\sigma_{\gamma\gamma'}$ can be obtained from all ground-state transitions of these lower-lying states. For many even-even nuclei the level density at small excitation energies is rather low. If higher-lying states decay exclusively (predominantly) via the 2_1^+ state, the intensity of the $2_1^+ \rightarrow 0_1^+$ transition contains (almost) the full *inelastic* cross section $\sigma_{\gamma\gamma'}$; see, e.g., Ref. [79]. Furthermore, if the intensity is collected in one transition, the sensitivity limit is increased compared to many separate ground-state transitions. However,

for the odd-even nucleus ^{87}Rb more than 20 excited states were observed up to 4 MeV by Käubler *et al.* [73] and all of these states predominantly decay directly back to the ground state. Hence, all of these transitions have to be observed to obtain the (almost) complete *inelastic* cross section $\sigma_{\gamma\gamma'}$. Moreover, the intensity ratio of energy-integrated cross sections of the bremsstrahlung measurements at $E_{e^-} = 8.2$ MeV and $E_{e^-} = 13.2$ MeV indicates *inelastic* transitions of states above 8 MeV to lower-lying excited states up to ≈ 5 MeV; see Fig. 3. The great advantage of the analysis of the photoabsorption cross section at HI γ S is the narrow energy resolution of the beam. Therefore, ground-state transitions can be identified and clearly distinguished from inelastic decays in a model-independent way. However, some inelastic channels might be below the sensitivity limit, and, thus, average branching ratios $\langle b_0 \rangle$ detected at HI γ S can be interpreted as a model-independent upper limit. However, the achievement of the selectivity in excitation energy compared to bremsstrahlung experiments is paid off by less beam time per excitation energy due to the energy scan that has to be performed with monoenergetic beams. In the case of ^{87}Rb the transition at 403 keV contributes the largest part to the observed inelastic cross section for every beam energy. The atomic background in this energy region is very large and the sensitivity limit is poor. An upper limit following the definition of Ref. [80] was determined for the transitions at 403, 845, 1389, and 1740 keV if not observed. At around 9.0 MeV the sum of these transitions accounts for $\approx 70\%$ of the observed inelastic cross section. Moreover, the transition at 1463 keV was not observable for all beam-energy settings, because of the dominant background transition at 1460.8 keV (decay of ^{40}K) and no upper limit can be estimated.

The photoabsorption cross section can also be analyzed directly from the bremsstrahlung measurement where the target nucleus is excited simultaneously in a wide excitation energy range for the complete beam time duration, which enables higher statistics. But, consequently, the γ -ray intensity in the bremsstrahlung spectrum cannot be assigned to elastic or inelastic decays in a model-independent way. Therefore, a well-established statistical approach was chosen to disentangle ground-state decays from other cascades. A detailed description of this method can be found in, e.g., Refs. [39,75]. Using the code MCGCS [81], 1000 nuclear realizations, each starting with an excitation from the ground state that is included in this code, were created with level densities derived from a global fitting to experimental data [82]. Also for the low-energy part of the level scheme the statistical methods were applied and fluctuations of the partial widths were treated by the Porter-Thomas distribution [83]. In the calculations the back-shifted Fermi-gas (BSFG) model was used. This allows a systematic comparison to the other $N = 50$ isotones where the same level density model was applied [35–38]. In the individual nuclear realizations parameters $a = 9.69(14)$ MeV $^{-1}$ and $E_1 = 0.11(7)$ MeV from empirical formulas based on global fits to experimental data were used [82], and a and E_1 were varied within their uncertainties. Equal level densities for states with positive and negative parity quantum numbers of the same spin quantum number were assumed. The resulting photoabsorption

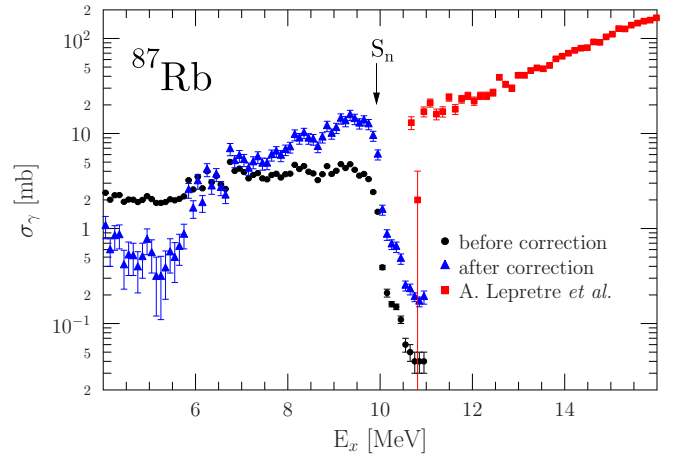


FIG. 6. Photoabsorption cross sections determined from the γ ELBE data before (black dots) and after correction for inelastic transitions and branching ratios (blue triangles). The (γ, n) data are illustrated with red squares [78].

cross sections are illustrated in Fig. 6 before correction for inelastic transitions (black dots) and after correction (blue triangles). It should be noted that the quoted uncertainties do not include potential systematic errors connected to the choice of level-density model. Additionally, (γ, n) data from Lepretre *et al.* are depicted with red squares [78]. The average branching ratio $\langle b_0 \rangle$ per energy bin ($\Delta = 100$ keV) and its errors are illustrated in Fig. 7(c) with blue lines. The resulting *elastic* photoabsorption cross section $\sigma_{\gamma\gamma}$ and the total photoabsorption cross section σ_γ after the disentanglement of the bremsstrahlung data using the code MCGCS [81] are illustrated in Figs. 7(b) and 7(a) with blue triangles. In Fig. 7(c) the values for $\langle b_0 \rangle$ that were derived from the HI γ S data are illustrated with red dots. The average branching ratios $\langle b_0 \rangle$ determined from the two different approaches do not agree within their uncertainties. The simulated branching ratios are in general smaller than those deduced from the measurements at HI γ S. The difference may be caused on the one hand by uncertainties of the level density parameters used in the statistical approach and, on the other hand, by missing intensities of transitions following inelastic decays that were not observed in the HI γ S spectra. For the higher beam energies, the ground-state transitions of almost all levels that have been observed by Käubler *et al.* were observed but no ground-state decays from states above 3.9 MeV. Moreover, the feeding behavior of the bremsstrahlung data at different endpoint energies indicates a non-negligible contribution of inelastic decays to excited states up to ≈ 5 MeV. The two lowest-lying ground-state transitions are at $E_\gamma = 403$ keV and $E_\gamma = 845$ keV. At these γ -ray energies the atomic background in the spectra is large and, therefore, the sensitivity limit is poor. At the lowest beam energies at HI γ S, no inelastic decays were observed. An upper limit for the ground-state transitions of the four first excited states ($E_\gamma = 403, 845, 1389, 1740$ keV) would yield values of $\langle b_0 \rangle < 0.2$ and, thus, provides no valuable information. Following these observations, the values of $\langle b_0 \rangle$ extracted from the HI γ S data support the statistical approach but do not provide a stringent proof.

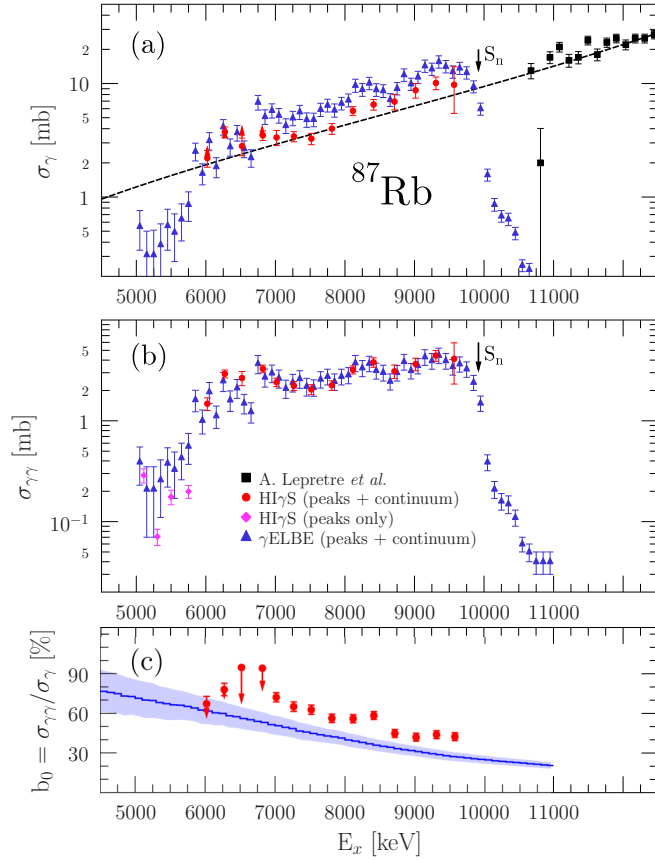


FIG. 7. The photoabsorption cross sections σ_γ of ^{87}Rb determined from the γELBE data (blue triangles) and the $\text{HI}\gamma\text{S}$ data (red dots) as well as the (γ, n) data (black squares) [78] with the associated standard Lorentzian (SLO) are illustrated in (a). The elastic part of the photoabsorption cross section $\sigma_{\gamma\gamma}$ is shown in (b). The average branching ratios to the ground state $\langle b_0 \rangle$ from the statistical approach (blue line) and the model-independent $\text{HI}\gamma\text{S}$ data (red dots) are depicted in (c). For details see text.

For the ground-state transitions the experimental asymmetry A provides information on the $E1/M1$ ratio. For the odd-even nucleus ^{87}Rb with ground-state spin $3/2^-$ angular distributions are less pronounced compared to even-even nuclei, and analyzing powers $\Sigma = 0, \pm 0.26, \pm 0.23$ are observed for states with spin and parity quantum numbers $J_i^\pi = 1/2^\mp, 3/2^\mp, 5/2^\mp$, respectively. However, average experimental asymmetries provide a tentative quantity for the $E1/M1$ ratio at every beam energy. For this purpose, the intensities in the deconvoluted HPGe detectors parallel and perpendicular to the polarization plane were determined detectorwise within the integral limit l and r (in analogy to Fig. 5). As a reference point ^{11}B (which has the same ground-state spin and parity quantum number as ^{87}Rb) was irradiated at a beam energy of 9.0 MeV. For the isolated strong $M1$ transition $3/2^- \rightarrow 5/2^- \rightarrow 3/2^-$ at $E_\gamma = 8917$ keV an azimuthal asymmetry of $A = 0.23(10)$ is observed. Due to the almost symmetric arrangement of the HPGe detectors an azimuthal asymmetry of $A = -0.23(10)$ for the respective $E1$ transition with an excited state of $J^\pi = 5/2^+$ is expected and

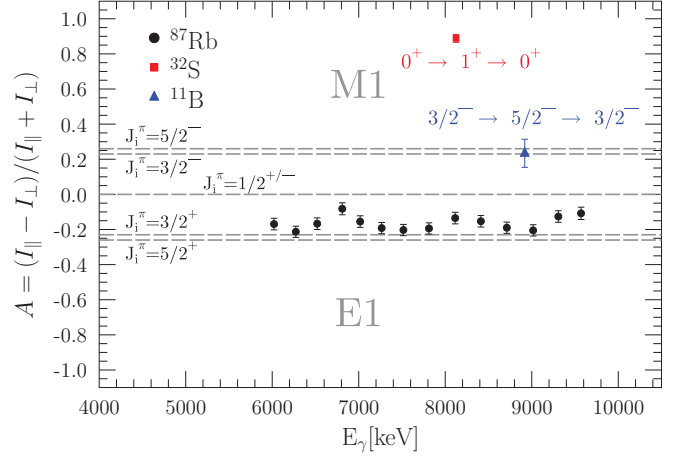


FIG. 8. Average experimental azimuthal asymmetries A per beam-energy setting measured at $\text{HI}\gamma\text{S}$ are illustrated for ^{87}Rb , ^{11}B , and ^{32}S with black dots, a blue triangle, and a red square, respectively. For details see text.

should be very similar to the $3/2^- \rightarrow 3/2^+ \rightarrow 3/2^-$ cascade (due to their very similar angular distributions). Only the transition $3/2^- \rightarrow 1/2^\pm \rightarrow 3/2^-$ is isotropic for $M1$ and $E1$ transitions. Observed azimuthal asymmetries A range from $-0.21(4)$ to $-0.08(4)$, which is in agreement with the assumption of almost pure $E1$ nature of the observed transitions but is not a stringent proof. The results for the azimuthal asymmetries A for ^{87}Rb are illustrated in Fig. 8 (black dots).

IV. DISCUSSION

A. The $^{86}\text{Rb}(n, \gamma)^{87}\text{Rb}$ cross section

In the following the new photoabsorption cross section data will be used to constrain the photon strength function (PSF) in ^{87}Rb and investigate its impact on the $^{86}\text{Rb}(n, \gamma)^{87}\text{Rb}$ cross section. Within the measurements, the average experimental azimuthal asymmetries A for every beam energy at $\text{HI}\gamma\text{S}$ agree with almost pure $E1$ strength with only minor $M1$ contributions; see Fig. 8. This observation is strengthened by observations in the neighboring even-even nucleus ^{86}Kr , where no isolated $M1$ transitions could be identified [38] from a measurement at $\text{HI}\gamma\text{S}$ with fully linearly polarized photons. Additionally, partly polarized bremsstrahlung photons were used to disentangle $E1$ and $M1$ contributions in ^{88}Sr where also no isolated $M1$ transitions were observed [36]. However, in both measurements $M1$ strength might be hidden in unresolved transitions. In the $N = 50$ isotope ^{90}Zr larger $M1$ contributions were observed [86]. The PSF of the other odd-even nucleus in the $N = 50$ chain ^{89}Y was measured via the Oslo method [57]. For the $^{88}\text{Y}(n, \gamma)^{89}\text{Y}$ and $^{88}\text{Sr}(p, \gamma)^{89}\text{Y}$ cross sections and rate calculations, Larsen *et al.* used a global parametrization for the $M1$ strength function peaking around 9.5 MeV, which will be adopted for the calculation of the $^{86}\text{Rb}(n, \gamma)^{87}\text{Rb}$ cross section. For the $E1$ strength function microscopic HFB+QRPA (Hartree-Fock-Bogoliubov plus quasiparticle random-phase approximation) calculations using the D1M interaction are used [84]. It

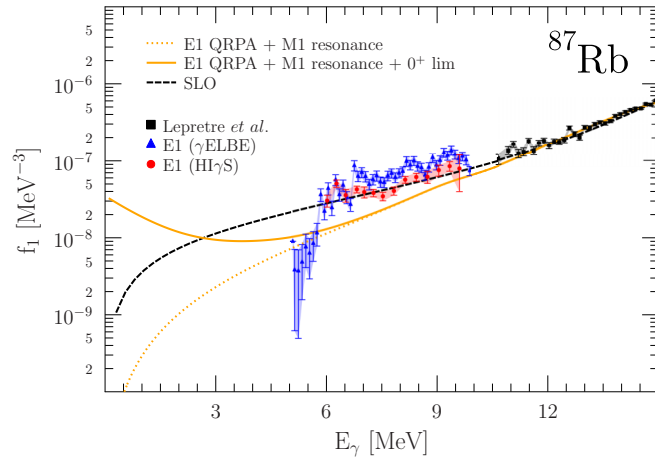


FIG. 9. The $E1$ -PSFs are illustrated for the results of the present work (red dots: $\text{HI}\gamma\text{S}$; blue triangles: γELBE). QRPA calculations as well as global parametrization for the $M1$ -PSF with (without) low-energy upbend are illustrated with orange solid (dotted) lines from Refs. [84,85]. The (γ, n) data are shown with black squares as well as their SLO parametrization (black dashed line) from Ref. [78]. For details see text.

was shown that these calculations in conjunction with global parametrizations for the low-energy part of the PSF globally reproduced experimental (n, γ) cross sections over the complete nuclear chart [85]. In the following the parametrization for the upper limit (“ 0^+ lim”) is used, which describes the total radiation widths $\langle \Gamma_\gamma \rangle$ globally with high accuracy [85]. First, the microscopic D1M HFB+QRPA calculations were renormalized (1.35) to (γ, n) data of Ref. [78]. The sum of these microscopic calculations for the $E1$ strength and the global $M1$ strength contribution is illustrated in Fig. 9 with orange continuous lines (with 0^+ lim) and orange dashed lines (without 0^+ lim). The experimental results of the photoabsorption data from the present work indicate a significant enhancement of strength between around 6 and 10 MeV compared to the microscopic D1M HFB+QRPA calculations. Then, the fraction of $M1$ strength is determined by the global parametrizations of $M1$ strength around 9.5 MeV and the low-energy part. The difference to experimental data is assumed to be of $E1$ type. Following these assumptions the $M1$ contribution amounts to about 10% around 8–10 MeV. It should be emphasized that the Brink-Axel hypothesis [90,91] is invoked to extract the PSF from the photoabsorption data. It presumes that the PSF depends only on the γ -ray energy of involved transitions independently of internal structures or the excitation energy of the nucleus. Isaak *et al.* observed a discrepancy between PSFs extracted from emission and absorption. However, this is mainly caused by transition energies below 6 MeV [77]. Also the D1M HFB+QRPA calculations are renormalized to (γ, n) photoabsorption data as outlined by Goriely *et al.* [85]. The average s -wave level spacing D_0 at the neutron separation energy S_n is a crucial input for the calculation of neutron capture cross sections. Whereas D_0 of stable target nuclei can be obtained from the available experimental set of s -wave resonances this is not feasible for unstable nuclei. With the

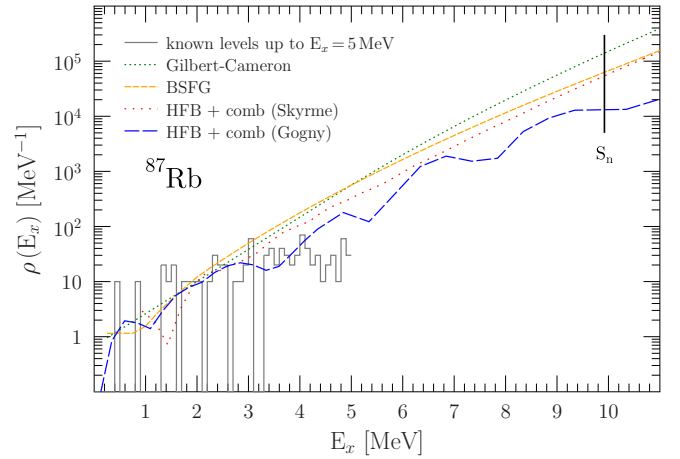


FIG. 10. The NLDs given by the Gilbert-Cameron model [87] (green, close-dotted line) and the BSFG model (orange, short-dashed line) as well as from microscopic Hartree-Fock-Bogolyubov calculations based on the Skyrme (red, wide-dotted line) and Gogny (blue, long-dashed line) forces are shown [88,89]. Known levels are illustrated in 100 keV bins with black lines [62]. For details see text.

Oslo method nuclear level densities (NLDs) can be obtained for a large energy range and are normalized to known levels; see, e.g., Refs. [57,92–94]. However, also a proper spin distribution $g(E_x, J)$ is unambiguous to correlate the total level density $\rho(E_x)$ and the s -wave level spacing D_0 . Moreover, additional information, e.g., on proton-capture reactions, provides valuable information on partial and total cross sections as well as PSFs extracted via the ratio method [95]. Nuclear level densities used in statistical model calculations can then be adjusted to match these experimentally observed variables; see, e.g., [95–97]. Also levels at low excitation energies should be accurately described by the level-density models. Because no Oslo-type experiments for ^{87}Rb as well as no $^{86}\text{Kr}(p, \gamma)^{87}\text{Rb}$ data are available, NLD models are only compared to known levels at low energies [62]. A phenomenological approach to describe the NLD is given by the Gilbert-Cameron model [87] which features a Gaussian spin distribution and equal parity (TALYS-1.9 [98] keyword *ldmodel 1*). Moreover, the BSFG model with the previously introduced parametrization is used (TALYS-1.9 keyword *ldmodel 2*). In contrast, several combinatorial approaches based on microscopic Hartree-Fock-Bogolyubov (“HFB + comb”) calculations are implemented in the TALYS-1.9 code [98] based on the Skyrme and D1M+Gogny interactions (TALYS-1.9 keywords *ldmodel 5* and *ldmodel 6*) [88,89]. For the latter one, varying nuclear properties at higher excitation energies are taken into account by a temperature dependency [89]. In contrast to the Gilbert-Cameron model, both microscopic approaches provide spin- and parity-dependent NLDs, and adjustment flexibility in the TALYS-1.9 code [98] is given by the scaling parameter α and the pairing shift δ [88]. The standard adjustment implemented in the TALYS-1.9 code was used ($\alpha = 0$ for both models and $\delta = 0.6811, -0.65637$ for *ldmodels 5,6*). The NLD models are illustrated in Fig. 10.

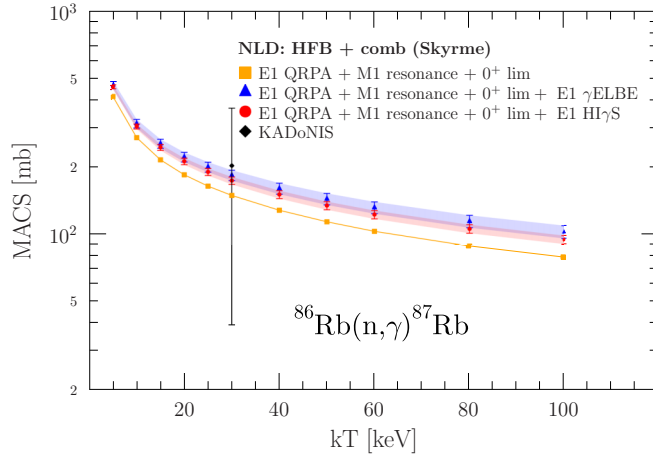


FIG. 11. The MACSs are illustrated for different PSF inputs, see Fig. 9. The PSF is held constant (*ldmodel* 5). The black diamond depicts the recommended value of the KADoNIS project [61]. For details see text.

Although all NLD models describe the first excited states up to 3 MeV quite well, their extrapolations to S_n show large deviations, and no normalization points are available. The values of D_0 are 67.67, 170.58, 216.47, 770.37 eV for *ldmodels* 1,2,5,6.

The influence of the additional strength deduced from (γ, γ') with respect to the $^{86}\text{Rb}(n, \gamma)^{87}\text{Rb}$ Maxwellian averaged cross section (MACS) is illustrated in Fig. 11. For this purpose the NLD is fixed [*“HFB + comb (Skyrme)”*]. The additional strength significantly enhances the values for the calculated MACSs, yielding crucial information for statistical model calculations of the s process involving the branching-point nucleus ^{86}Rb . Additionally, the influence of the NLD is depicted in Fig. 12. For this purpose, the PSF is fixed (*E1 QRPA + M1 resonance + 0⁺ lim + E1 HIγS*). The different

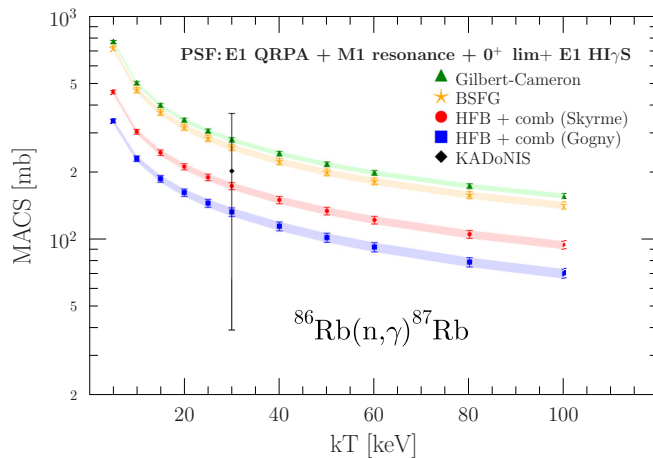


FIG. 12. The MACSs are illustrated for different NLD models; cf. Fig. 10. The PSF is hold constant (*E1 QRPA + M1 resonance + 0⁺ lim + E1 HIγS*); cf. Fig. 9. The black diamond depicts the recommended value of the KADoNIS project [61]. For details see text.

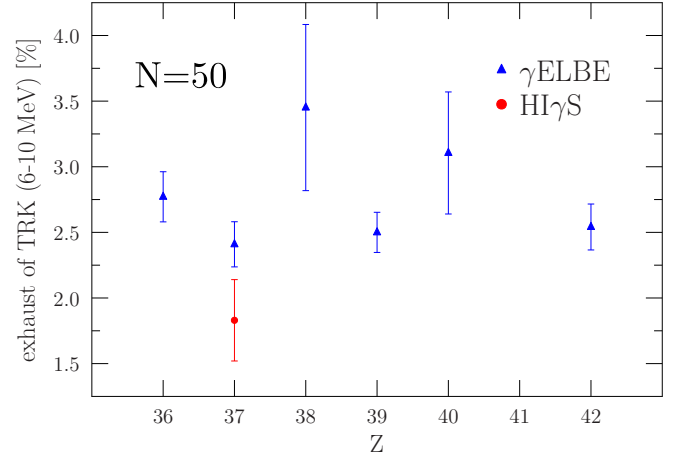


FIG. 13. The fraction of the TRK sum rule between 6 and 10 MeV is illustrated for the $N = 50$ isotones. Values extracted directly from γELBE data are illustrated with blue triangles [35–39]. For ^{87}Rb the value determined at $\text{HI}\gamma\text{S}$ is illustrated with a red dot. For details see text.

NLDs cause large deviations of the calculated MACSs. However, the recommended value of the KADoNIS project could be improved [61].

Nevertheless, further measurements of the PSF of ^{87}Rb are important to experimentally constrain the low-energy part of the PSF as well as the NLD at higher excitation energies which are not accessible from (γ, γ') experiments. For this purpose, Oslo type experiments are a powerful tool; see, e.g., Refs. [57,92–94]. Moreover, the extraction of PSFs from proton-capture experiments may shed light on the accordance between several techniques. For the PSF of ^{89}Y extracted via the Oslo method experimental data of Galanopoulos *et al.* for the $^{88}\text{Sr}(p, \gamma)^{89}\text{Y}$ reaction could be well reproduced [57,99]. However, for ^{90}Zr results between the PSF extracted from (γ, γ') experiments and the PSF extracted from a $^{89}\text{Y}(p, \gamma)^{90}\text{Zr}$ show deviations for some energies [100]. Thus, the $^{86}\text{Kr}(p, \gamma)^{87}\text{Rb}$ in-beam measurement will probably yield important information on the PSF in ^{87}Rb [95,101]. If the present results will be completed by other techniques covering the complete energy range of the PSF, also the influence of other input parameters, e.g., the neutron optical-model potential, should be examined.

B. The evolution of dipole strength in the $N = 50$ isotones

At excitation energies above 6 MeV the dipole response of the $N = 50$ isotones has been elaborated from Kr to Mo by means of photon-scattering experiments [35–39], and a detailed discussion for the even-even isotopes can be found in Ref. [38]. The present measurements fill the gap for ^{87}Rb . The fraction of the TRK sum rule between 6 and 10 MeV amounts to 2.41(17)% and 1.83(31)% for the analysis of the γELBE data and $\text{HI}\gamma\text{S}$ data, respectively. The evolution of the fraction of dipole strength between 6 and 10 MeV from the TRK sum rule is illustrated in Fig. 13. Along the $N = 50$ isotones no clear trend for the exhaust of the TRK sum rule is observed. Some part of the inelastic cross sections at $\text{HI}\gamma\text{S}$ might not

be observed as they might be below the sensitivity limit of the experiment. Therefore, both approaches do not contradict, but also no final conclusion can be drawn.

V. SUMMARY AND OUTLOOK

The photoabsorption cross section of ^{87}Rb was measured in two bremsstrahlung measurements with electron energies of $E_{e^-} = 13.2$ MeV and $E_{e^-} = 8.2$ MeV at the γELBE facility. The energy-integrated cross sections for more than 200 dipole excited states were found between 4 and 10 MeV for the first time in photon scattering experiments. The photoabsorption cross sections were determined by a statistical and a model-independent approach. The bremsstrahlung experiments were complemented by an energy scan using monochromatic photon beams at the HI γ S facility. Model-independent average branching ratios $\langle b_0 \rangle$ were extracted for every beam-energy setting and can be interpreted as an upper limit as some bypass transition might be below the sensitivity limit. Therefore, the extracted photoabsorption cross sections σ_γ at HI γ S serve as lower limit. Moreover, average azimuthal asymmetries A determined at HI γ S support dominant electric type

of radiation, which is in agreement with results in the even-even neighbors ^{86}Kr and ^{88}Sr . The extracted PSFs from the present (γ, γ') measurements on ^{87}Rb were used to constrain the $^{86}\text{Rb}(n, \gamma)^{87}\text{Rb}$ cross section. Additional $E1$ strength between 6 and 10 MeV significantly enhances calculated MACSs and, thus, might play a crucial role for the s -process waiting-point nucleus ^{86}Rb . Further experiments are important to constrain the NLD at higher energies as well as the PSF at lower energies.

ACKNOWLEDGMENTS

We thank the HI γ S operators and γELBE operators for providing excellent photon beams for our experiment. We thank A. Blazhev and K. O. Zell for the target preparation. This work was supported by the BMBF (05P18PKEN9), by the U.S. Department of Energy, Office of Nuclear Physics under Grant No. DE-FG02-97ER41033, and by the Alliance Program of the Helmholtz Association (HA216/EMMI). U.F.G. acknowledges support by the Deutsche Forschungsgemeinschaft (DFG) under Grant No. SFB 1245 (Project ID 279384907).

- [1] D. Savran, T. Aumann, and A. Zilges, *Prog. Part. Nucl. Phys.* **70**, 210 (2013).
- [2] K. Heyde, P. von Neumann-Cosel, and A. Richter, *Rev. Mod. Phys.* **82**, 2365 (2010).
- [3] M. Harakeh and A. von der Woude, *Giant Resonances* (Oxford University Press, Oxford, 2001).
- [4] F. Reiche and W. Thomas, *Z. Phys.* **34**, 510 (1925).
- [5] W. Kuhn, *Z. Phys.* **33**, 408 (1925).
- [6] B. L. Berman and S. C. Fultz, *Rev. Mod. Phys.* **47**, 713 (1975).
- [7] R. Bergère, in *Photonuclear Reactions I*, International School on Electro- and Photonuclear Reactions, Erice, Italy 1976, edited by S. Costa and C. Schaerf, Lecture Notes in Physics Vol. 61 (Springer, Berlin, 1977), p. 1.
- [8] A. Tamii *et al.*, *Nucl. Instrum. Methods Phys. A* **605**, 326 (2009).
- [9] R. Neveling *et al.*, *Nucl. Instrum. Methods Phys. A* **654**, 29 (2011).
- [10] P. von Neumann-Cosel and A. Tamii, *Eur. Phys. J. A* **55**, 110 (2019).
- [11] B. Özel-Tashenov *et al.*, *Phys. Rev. C* **90**, 024304 (2014).
- [12] L. Pellegri *et al.*, *Phys. Lett. B* **738**, 519 (2014).
- [13] K. Govaert, F. Bauwens, J. Bryssinck, D. De Frenne, E. Jacobs, W. Mondelaers, L. Govor, and V. Y. Ponomarev, *Phys. Rev. C* **57**, 2229 (1998).
- [14] J. Endres *et al.*, *Phys. Rev. Lett.* **105**, 212503 (2010).
- [15] H. K. Toft *et al.*, *Phys. Rev. C* **83**, 044320 (2011).
- [16] Krumbholz *et al.*, *Phys. Lett. B* **744**, 7 (2015).
- [17] M. Müsscher *et al.*, *Phys. Rev. C* **102**, 014317 (2020).
- [18] R. Massarczyk *et al.*, *Phys. Rev. Lett.* **112**, 072501 (2014).
- [19] F. Bauwens *et al.*, *Phys. Rev. C* **62**, 024302 (2000).
- [20] T. Hartmann, J. Enders, P. Mohr, K. Vogt, S. Volz, and A. Zilges, *Phys. Rev. C* **65**, 034301 (2002).
- [21] T. Hartmann, M. Babilon, S. Kamerdzhiev, E. Litvinova, D. Savran, S. Volz, and A. Zilges, *Phys. Rev. Lett.* **93**, 192501 (2004).
- [22] J. Isaak *et al.*, *Phys. Rev. C* **83**, 034304 (2011).
- [23] M. Scheck *et al.*, *Phys. Rev. C* **87**, 051304(R) (2013).
- [24] K. Govaert *et al.*, *Nucl. Instrum. Methods Phys. A* **337**, 265 (1994).
- [25] H. Pai *et al.*, *Phys. Rev. C* **88**, 054316 (2013).
- [26] Krishichayan, M. Bhihe, W. Tornow, G. Rusev, A. P. Tonchev, N. Tsoneva, and H. Lenske, *Phys. Rev. C* **91**, 044328 (2015).
- [27] J. Wilhelmy *et al.*, *Phys. Rev. C* **98**, 034315 (2018).
- [28] P. C. Ries *et al.*, *Phys. Rev. C* **100**, 021301(R) (2019).
- [29] R.-D. Herzberg *et al.*, *Phys. Lett. B* **390**, 49 (1997).
- [30] R.-D. Herzberg *et al.*, *Phys. Rev. C* **60**, 051307(R) (1999).
- [31] N. Pietralla *et al.*, *Phys. Rev. Lett.* **88**, 012502 (2001).
- [32] A. Zilges, S. Volz, M. Babilon, T. Hartmann, P. Mohr, and K. Vogt, *Phys. Lett. B* **542**, 43 (2002).
- [33] D. Savran, M. Fritzsche, J. Hasper, K. Lindenberg, S. Müller, V. Y. Ponomarev, K. Sonnabend, and A. Zilges, *Phys. Rev. Lett.* **100**, 232501 (2008).
- [34] B. Löher *et al.*, *Phys. Lett. B* **756**, 72 (2016).
- [35] N. Benouaret *et al.*, *Phys. Rev. C* **79**, 014303 (2009).
- [36] R. Schwengner *et al.*, *Phys. Rev. C* **76**, 034321 (2007).
- [37] R. Schwengner *et al.*, *Phys. Rev. C* **78**, 064314 (2008).
- [38] R. Schwengner *et al.*, *Phys. Rev. C* **87**, 024306 (2013).
- [39] G. Rusev *et al.*, *Phys. Rev. C* **79**, 061302(R) (2009).
- [40] U. Kneissl, H. H. Pitz, and A. Zilges, *Prog. Part. Nucl. Phys.* **37**, 349 (1996).
- [41] J. Endres, D. Savran, A. M. van den Berg, P. Dendooven, M. Fritzsche, M. N. Harakeh, J. Hasper, H. J. Wörtche, and A. Zilges, *Phys. Rev. C* **80**, 034302 (2009).
- [42] M. Krzysiek *et al.*, *Phys. Rev. C* **93**, 044330 (2016).
- [43] D. Savran *et al.*, *Phys. Lett. B* **786**, 16 (2018).
- [44] A. Bracco, E. G. Lanza, and A. Tamii, *Prog. Part. Nucl. Phys.* **106**, 360 (2019).
- [45] V. Derya *et al.*, *Phys. Rev. C* **93**, 034311 (2016).
- [46] R.-D. Herzberg *et al.*, *Nucl. Phys. A* **592**, 211 (1995).
- [47] M. Wilhelm, E. Radermacher, A. Zilges, and P. von Brentano, *Phys. Rev. C* **54**, R449 (1996).

- [48] W. Andrejtscheff, C. Kohstall, P. Von Brentano, C. Fransen, U. Kneissl, N. Pietralla, and H. H. Pitz, *Phys. Lett. B* **506**, 239 (2001).
- [49] S. Goriely, *Phys. Lett. B* **436**, 10 (1998).
- [50] S. Goriely *et al.*, *Eur. Phys. J. A* **55**, 172 (2019).
- [51] H. Utsunomiya *et al.*, *Phys. Rev. C* **80**, 055806 (2009).
- [52] H. Utsunomiya *et al.*, *Phys. Rev. C* **81**, 035801 (2010).
- [53] H. Utsunomiya *et al.*, *Phys. Rev. C* **84**, 055805 (2011).
- [54] H. Utsunomiya *et al.*, *Phys. Rev. C* **100**, 034605 (2019).
- [55] R. Massarczyk *et al.*, *Phys. Rev. C* **87**, 044306 (2013).
- [56] R. Massarczyk *et al.*, *Phys. Rev. C* **93**, 014301 (2016).
- [57] A. C. Larsen *et al.*, *Phys. Rev. C* **93**, 045810 (2016).
- [58] F. Käppeler, R. Gallino, S. Bisterzo, and W. Aoki, *Rev. Mod. Phys.* **83**, 157 (2011).
- [59] M. Lugaro and A. Chieffi, in *Astrophysics with Radioactive Isotopes*, Astrophysics and Space Science Library, Vol. 453, edited by R. Diehl, D. H. Hartmann, and N. Prantzos (Springer, Cham, 2018), pp. 91–172.
- [60] C. Arlandini *et al.*, *Astrophys. J.* **525**, 886 (1999).
- [61] I. Dillmann, R. Plag, F. Käppeler, and T. Rauscher, KADONiS v0.3 - The third update of the Karlsruhe Astrophysical Database of Nucleosynthesis in Stars, available at <https://www.kadonis.org/>.
- [62] T. Johnson and W. Kulp, *Nucl. Data Sheets* **129**, 1 (2015).
- [63] M. Heil, F. Käppeler, E. Uberseder, R. Gallino, S. Bisterzo, and M. Pignatari, *Phys. Rev. C* **78**, 025802 (2008).
- [64] R. Schwengner *et al.*, *Nucl. Instrum. Methods Phys. A* **555**, 211 (2005).
- [65] H. R. Weller, M. W. Ahmed, H. Gao, W. Tornow, Y. K. Wu, M. Gai, and R. Miskimen, *Prog. Part. Nucl. Phys.* **62**, 257 (2009).
- [66] B. Löher *et al.*, *Nucl. Instrum. Methods Phys. A* **723**, 136 (2013).
- [67] S. Agostinelli *et al.*, *Nucl. Instrum. Methods Phys. A* **506**, 250 (2003).
- [68] J. Allison *et al.*, *IEEE Trans. Nucl. Sci.* **53**, 270 (2006).
- [69] J. Allison *et al.*, *Nucl. Instrum. Methods Phys. A* **835**, 186 (2016).
- [70] G. Roche, C. Ducos, and J. Proriot, *Phys. Rev. A* **5**, 2403 (1972).
- [71] L. I. Schiff, *Phys. Rev.* **83**, 252 (1951).
- [72] G. Rusev, A. P. Tonchev, R. Schwengner, C. Sun, W. Tornow, and Y. K. Wu, *Phys. Rev. C* **79**, 047601 (2009).
- [73] L. Käubler *et al.*, *Phys. Rev. C* **65**, 054315 (2002).
- [74] See Supplemental Material at <http://link.aps.org/supplemental/10.1103/PhysRevC.102.044327> for isolated states and branching ratios.
- [75] T. Shizuma *et al.*, *Phys. Rev. C* **98**, 064317 (2018).
- [76] J. Isaak *et al.*, *Phys. Lett. B* **727**, 361 (2013).
- [77] J. Isaak *et al.*, *Phys. Lett. B* **788**, 225 (2019).
- [78] A. Lepretre, H. Beil, R. Bergere, P. Carlos, A. Veyssiere, and M. Sugawara, *Nucl. Phys. A* **175**, 609 (1971).
- [79] A. P. Tonchev, S. L. Hammond, J. H. Kelley, E. Kwan, H. Lenske, G. Rusev, W. Tornow, and N. Tsoneva, *Phys. Rev. Lett.* **104**, 072501 (2010).
- [80] J. Endres *et al.*, *Phys. Rev. C* **85**, 064331 (2012).
- [81] G. Rusev, Ph.D. dissertation, Technische Universität Dresden, 2007 (unpublished) (Wissenschaftlich-Technische Berichte, FZD-478, 2007).
- [82] T. von Egidy and D. Bucurescu, *Phys. Rev. C* **72**, 044311 (2005).
- [83] C. E. Porter and R. G. Thomas, *Phys. Rev.* **104**, 483 (1956).
- [84] M. Martini, S. Péru, S. Hilaire, S. Goriely, and F. Lechaftois, *Phys. Rev. C* **94**, 014304 (2016).
- [85] S. Goriely, S. Hilaire, S. Péru, and K. Sieja, *Phys. Rev. C* **98**, 014327 (2018).
- [86] G. Rusev *et al.*, *Phys. Rev. Lett.* **110**, 022503 (2013).
- [87] A. Gilbert and A. G. W. Cameron, *Can. J. Phys.* **43**, 1446 (1965).
- [88] S. Goriely, S. Hilaire, and A. J. Koning, *Phys. Rev. C* **78**, 064307 (2008).
- [89] S. Hilaire, M. Girod, S. Goriely, and A. J. Koning, *Phys. Rev. C* **86**, 064317 (2012).
- [90] D. M. Brink, Doctoral thesis, University of Oxford, 1955 (unpublished).
- [91] P. Axel, *Phys. Rev.* **126**, 671 (1962).
- [92] A. C. Larsen and S. Goriely, *Phys. Rev. C* **82**, 014318 (2010).
- [93] T. Renstrøm *et al.*, *Phys. Rev. C* **93**, 064302 (2016).
- [94] I. K. Kullmann *et al.*, *Phys. Rev. C* **99**, 065806 (2019).
- [95] F. Heim, J. Mayer, M. Müller, P. Scholz, M. Weinert, and A. Zilges, *Nucl. Instrum. Methods Phys. A* **966**, 163854 (2020).
- [96] F. Heim, P. Scholz, M. Korschgen, J. Mayer, M. Müller, and A. Zilges, *Phys. Rev. C* **101**, 035805 (2020).
- [97] F. Heim, P. Scholz, J. Mayer, M. Müller, and A. Zilges, *Phys. Rev. C* **101**, 035807 (2020).
- [98] A. J. Koning and D. Rochman, *Nucl. Data Sheets* **113**, 2841 (2012).
- [99] S. Galanopoulos *et al.*, *Phys. Rev. C* **67**, 015801 (2003).
- [100] L. Netterdon, A. Endres, S. Goriely, J. Mayer, P. Scholz, M. Spieker, and A. Zilges, *Phys. Lett. B* **744**, 358 (2015).
- [101] L. Netterdon *et al.*, *Nucl. Instrum. Methods Phys. A* **754**, 94 (2014).